Chalcopyrite solar cells
—state-of-the-art and options for improvement

S. Siebentritt[*], and T. P. Weiss[*]

Laboratory for Photovoltaics, Department of Physics and Materials Science, University of Luxembourg, Belvaux 4422, Luxembourg

Chalcopyrite solar cells will have to play an important role to mitigate the climate crisis, because of their particularly low carbon emissions. Doping in these semiconductors is due to native defects and intentional alkali impurities. The recent progress in efficiency has been made possible by post-deposition treatments with heavy alkalis. Tail states and band gap distribution are the main limitations for the open circuit voltage in state-of-the-art chalcopyrite solar cells. Further efficiency limitations are due to the increased diode factor because of metastable defect transitions. Alloying with Ag opens new possibilities of band-edge engineering, as well as seems to improve the diode factor. In state-of-the-art cells the back contact is passivated by a Ga gradient; considerable research has been done to passivate the back contact by structured or continuous dielectric layers. A leap forward in efficiency can be expected from tandem cells. Chalcopyrite solar cells show promising potential as bottom cells as well as top cells.

doping, tail states, alkali treatment, efficiency

PACS number(s): 71.20.Nr, 71.55.Ht, 81.05.Hd, 84.60.Jt

1   Introduction: Why we need thin film solar cells

The recent IPCC (Intergovernmental Panel on Climate Change) report lists solar energy as most effective and cost-efficient tool to mitigate the climate crisis (IPCC. Climate Change 2022-Mitigation of Climate Change-Summary for Policymakers, https://report.ipcc.ch/ar6wg3/pdf/IPCC_AR6 _WGIII_SummaryForPolicymakers.pdf), although the technical potential of PV (photovoltaics) has long been underestimated [1]. Various studies on a climate neutral energy system of the future come to the conclusion that photovoltaics will have to be one of the major electricity sources [2] (IRENA International Renewable Energy Agency. World Energy Transitions Outlook 2022: 1.5°C Pathway-Executive summary, https://www.irena.org/publications/2022/Mar/World-Energy-Transitions-Outlook-2022), necessitating a huge increase in the annual PV installations [1]. To achieve this goal without increasing green house gas (GHG) emissions it is necessary to reduce the GHG emissions during the production of PV modules. A 2016 report by the UNEP (United Nations' Environment Programme) compared the green house gas emissions by different energy sources [3] using the then available data and technology projections. Already this report confirms that solar PV electricity has one to two orders of magnitude lower GHG emissions than any fossil based power station. Furthermore, the study predicts for the 2030 technologies GHG emissions for Si solar cells of slightly above 30 g CO_2e/kW h. It can be stated, that also in this

*Corresponding authors (S. Siebentritt, email: susanne.siebentritt@uni.lu; T. P. Weiss, email: thomas.weiss@uni.lu)

respect, the potential of PV is underestimated. In fact, today's state-of-the-art Si solar modules emit only 13 to 30 g CO_2e/kW h [4]. A similar study on state-of-the-art thin film solar cells is missing. However, a 2018 study on current Cu chalcopyrite solar modules produced on stainless steel, using different scenarios found in the best case GHG emissions of 5 g CO_2e/ kW h [5]. Also the mentioned UNEP study [3] found in direct comparison to Si solar cells that thin film solar cells emit a factor 3 to 5 less GHG. Furthermore, a recent long term study found that the performance ratio of $Cu(In,Ga)Se_2$ modules, calibrated to 25°C, was the best among all investigated modules, which included several state-of-the-art Si modules, as well as CdTe modules [6]. Therefore, it is highly desirable to install considerably more PV systems to mitigate the climate crisis and in particular to install more thin film PV systems. Thin film solar cells based on chalcopyrite absorbers are commercially available. The technology is particularly suited for building integration [7], as well as for utility systems. Chalcopyrite solar modules have proven stable in the field over decades (for detailed investigations see e.g., refs. [8,9]), as well as in accelerated aging test [7]. Recently the efficiency of this technology has been increased to 23.4% in the laboratory [10] and 19.8% on the module level (Avancis. https://www.avancis.de/en/magazine/pr-efficiency). Several companies in Europe, the US and Asia produce chalcopyrite modules, either as glass-glass devices or as flexible products on steel or plastic foil. Production is still relatively small at 1.5 GW per year (Fraunhofer ISE. Photovoltaics Report, https://www.ise.fraunhofer. de/en/publications/studies/photovoltaics-report.html), but its potential for GHG reduction should be a good argument to increase production. In this article we give an overview on recent scientific and technological developments of chalcopyrite PV solar cells and modules.

2   A short overview of recent reviews

"Chalcopyrite" describes the tetragonal crystal structure of I-III-VI$_2$ compounds. $Cu(In,Ga)Se_2$ is an alloy of $CuInSe_2$ and $CuGaSe_2$ with a bandgap varying with the Ga content between 1.0 and 1.65 eV. Also alloys with S, replacing partly or completely Se, and with Ag, replacing partly Cu are used as solar cell absorbers. These compounds are discussed in sect. 6 and 8. Collectively, these materials are often labelled "CIGS" or "CIS". A number of excellent reviews exist on material properties and solar cell technology. Fundamental structural and electronic properties of these materials are summarised in an early book by Shay and Wernick [11]. A recent review on crystal and band structure by Wada can be found in ref. [12]. The historical development of the technology is available in refs. [8,13]. Important aspects of the historical efficiency improvement were the introduction of a

band gap gradient, based on a Ga profile [14], which helps to reduce interface recombination [15,16] and the discovery that the presence of sodium improves the doping level of chalcopyrites [17,18]. Two recent reviews call for a paradigm change and propose to remove the Ga gradient in chalcopyrite solar cells and to implement selective contacts instead [19,20]. Both aspects are discussed in further detail below in sects. 4 and 7.

The technological state-of-the-art can be found in refs. [21,22], and a short review on the recent developments in ref. [23]. A discussion of issues concerning the efficiency of commercial modules has been presented in ref. [24]. A particular advantage of chalcopyrite solar cells is that they can be prepared on flexible substrates and made into bendable and lightweight modules [25,26].

3   Native defects and metastabilities

The structure of chalcopyrite solar cells is based on a p/n hetero junction between the p-type chalcopyrite and an n-type TCO (transparent conductive oxide). The advantages of hetero junctions for solar cells based on highly absorbing materials have been discussed in ref. [27]. The p-type doping of chalcopyrite absorbers is due to native defects and due to extrinsic doping by alkali impurities, which are discussed in sect. 5. Native defects have been studied by photoluminescence, admittance spectroscopy and by *ab initio* calculations. A recent review can be found in ref. [28]. We summarise the main results in Figure 1 and Table 1. The p-type doping in $CuInSe_2$ and $CuGaSe_2$ is dominantly caused by two acceptors, that have been identified as the Cu vacancy and the Cu-on-III antisite. Under certain conditions a third acceptor is present. Theses acceptors are compensated by shallow and deep donors, notably the Cu interstitial and the III-on-Cu antisite. The latter is shallow in $CuInSe_2$ and deep in $CuGaSe_2$. It is likely that this defect plays a role in the higher non-radiative loss in the open-circuit voltage, that is observed for high Ga $Cu(In,Ga)Se_2$ [28]. It has been found that Cu-rich chalcopyrite is higher doped than Cu-poor material [29-31]. Furthermore, it has been observed by photoluminescence that the luminescence due to A2 (Cu-on-III) increases with increasing Cu-content, whereas the luminescence due to A1 (Cu vacancy decreases) [32,33]—as one would expect. Thus, it appears, that Cu-rich material is mostly doped by the Cu-on-III antisite acceptor, however, Cu vacancy acceptors are still present in Cu-rich material. The lower doping in Cu-poor material is due to the fact, that the Cu vacancy acceptor is compensated by III-on-Cu antisite donor. In fact, it has been found by neutron scattering in $CuInSe_2$ that the concentration of Cu vacancies does not change much in the Cu-poor composition range, whereas the concentration of In-on-Cu antisite increases with decreasing
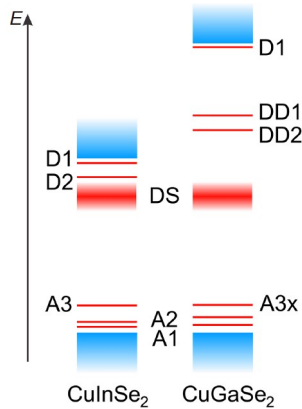
Figure 1 (Color online) Overview of native defects in Cu(In,Ga)Se$_2$. Physico-chemical structures are summarised in Table 1. From ref. [28] (reproduced under CCBY licence).

Table 1 Defect structures. According to ref. [28] (III: In or Ga)

Defect label	Defect structure
A1	Cu vacancy
A2	Cu-on-III antisite
A3	tentatively: In vacancy
A3x	unknown
D1	Cu interstitial, in CuInSe$_2$ also In-on-Cu antisite
D2	tentatively Se-Cu double vacancy
DD2	Ga-on-Cu antisite
DD1	tentatively: lower charge state of Ga on Cu antisite
DS	has been proposed tentatively as second charge state of Cu-on-III antisite

Cu content [34]. This behaviour implies an increasing degree of compensation and thus lower net doping with decreasing Cu content. Indeed, Cu-poor CuInSe$_2$ without Na and grown under low Se conditions, is n-type [35,36]. In the contrary, CuGaSe$_2$ is always p-type, independent of the composition. It was found that above around 17% Ga/Ga+In atomic ratio is needed in Cu(InGa)Se$_2$ to make the Cu-poor material p-type without Na doping [37].

While the shallow defects are responsible for the doping level and the degree of compensation, deep defects like the DS and the DD defects are clearly unwanted, because they act as recombination centres and decrease the quasi-Fermi level splitting and the open circuit voltage [38]. It is interesting to note that in all chalcopyrites, including the sulfide chalcopyrites, we observe the same deep level luminescence. The only difference is: with higher band gaps we observe more deep levels [39]. The luminescence related to the DS defect is found in all Cu(In,Ga)(S,Se)$_2$ chalcopyrites, the DD2 luminescence is observed in CuInS$_2$ and all chalcopyrites with a higher bandgap, DD1 luminesce in Cu(In,Ga)S$_2$ from a band gap of 1.6 eV upwards, as well as in CuGaSe$_2$. In CuGaS$_2$, which has the highest band gap of 2.5 eV, three

more deep defects are observed.

Another effect related to native defects is metastable behaviour. Metastabilities have been observed in Cu(In,Ga)Se$_2$ solar cells early on: light soaking describes the effect that the open circuit voltage increases with illumination time [40]. There exists a variety of metastable effects, some of them are clearly related to the buffer or the buffer/absorber interface [41-44]. Here, we concentrate on metastable effects related to the Cu(In,Ga)Se$_2$ absorber. Metastable effects are generally accompanied by an increase in the doping level [45], also visible as persistent photoconductivity [46]. First explanations already attributed these effects to amphoteric defects [47]. From a summary of the then available experimental data Rau et al. [48] proposed as early as 2001 that the metastable effects are related to Se vacancies. *Ab initio* calculations showed in fact that the Se vacancy does show metastable behaviour in various semiconductors due to the formation of cation dimers [49]. Breaking the bonding of these dimers requires considerable energy, which explains the metastable stabilisation of the charge state that forms the dimers. In Cu(In,Ga)Se$_2$, the Se vacancy forms a defect complex with the Cu vacancy. This defect shows metastable transitions between donor type and acceptor type [50], which can explain the metastable increase of the doping level. It was shown recently that Na and K play a role in the metastable increase of the doping level [51,52]. The In-on-Cu antisite has also been described as a metastable defect [53] which transitions from a shallow donor (the antisite) to a deep donor (a DX defect, where the In atom becomes interstitial) thereby trapping electrons. It should be noted, however, that more recent calculations found that the transition to the DX state is not likely under normal experimental conditions [54].

In particular the metastable increase of the doping level has been found to anneal out at temperature above about 200 K [52,55]. Thus, it could be expected that this metastable effects have little influence on solar cell efficiency. However, even at room temperature but under excitation there will be a steady-state quasi-equilibrium between the acceptor state and the donor state of the metastable defect. The balance between the two states will depend on the amount of excitation, i.e. illumination level or applied voltage. With higher excitation more metastable defects are in the acceptor state, thereby increasing the effective doping level. This behaviour of the metastable defects leads to a shift of the majority quasi-Fermi level, even in low injection conditions. Thus, metastable defects will increase the diode factor above 1 even for recombination in the quasi-neutral region and under low excitation conditions [56]. This diode factor increase can be most easily studied by the excitation dependence of the photoluminescence (PL) flux [57,58]. This "optical diode factor" measurement is essentially the same as a jV (current-voltage) measurement in forward direction: in a

jV measurement the voltage is applied and the current measured, whereas in the PL measurement the generation flux, i.e. the current, is fixed and the measured PL flux is determined by the quasi-Fermi level splitting, i.e., the voltage [58]. The increase in the diode factor by metastable defects has been confirmed experimentally and by simulations [56]. The effect of the metastable defects is summarised in Figure 2. We would like to note that without metastable defects, the diode factor for dominant recombination in the quasi-neutral zone is 1 because only the electron quasi-Fermi level shifts, whereas it is 2 for recombination in the space charge region, because here both Fermi levels shift with increasing excitation (by light or by voltage) [59]. In a PL experiment no contacts are applied to the absorber, i.e. no space charge region exists and recombination takes place in the neutral region. Thus, without metastable defects a diode factor of 1 would be expected in low excitation (Figure 2 left) [56].

A higher diode factor leads to a lower fill factor of the solar cell and thus to lower efficiency [59]. Although the increased doping level after light soaking anneals out at room temperature, the steady-state situation under continuous excitation between the acceptor and the donor state of the metastable defects shifts with excitation and thus shifts the majority quasi-Fermi level, increasing the diode factor and thereby decreasing the fill factor [60]. Thus, metastable defects do decrease the efficiency of solar cells. We recently found that alloying with Ag decreases metastable effects and increases the fill factor [60] (see also sect. 6).

4   Tail states

Besides deep defects, tail states also lead to losses in the open circuit voltage [61]. They lead to radiative and non-radiative losses [62]. In an ideal semiconductor the density of states in the bandgap is zero. However, in real semiconductors, band tails occur, which are characterised by a density of states, decaying exponentially into the gap. The decay constant is
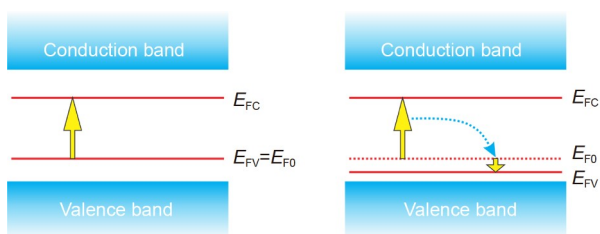

Figure 2 (Color online) p-type semiconductor under low excitation: without metastable defects (left) and with metastable defects (right). Without metastable defects only the electron quasi-Fermi level (E_{FC}) shifts, whereas in the presence of metastable defects an additional shift of the hole Fermi level (E_{FV}) occurs. This shift depends in turn on the electron concentration and increases the diode factor. E_{F0} depicts the equilibrium Fermi level. For more details see ref. [56].

called the Urbach energy [63-66]. Essentially, higher Urbach energies mean there are more tail states. The temperature dependence of the Urbach energy can be attributed to the vibrational disorder caused by phonons, while static disorder adds an additional constant contribution [64,67]. The static disorder is partly due to structural deviations from the ideal crystal like grain boundaries, or due to variations in the composition [68]. Grain boundaries contribute to tail states, as can be seen from the higher Urbach energy found in polycrystalline films than in single crystalline films [69], however the difference is rather small: Urbach energies vary between 10 and 17 meV between Cu-rich and Cu-poor $CuInSe_2$ and the Urbach energies of single crystalline films are only 1 or 2 meV lower than those of polycrystalline ones. It is also likely that bond length variations in the chalcopyrite crystal contribute to the tail states [70]. Furthermore, electrostatic fluctuations due to doping compensation will play a role in the formation of tail states. These fluctuations are greatly reduced at room temperature, but do not disappear completely [71]. The electrostatic band bending around charged grain boundaries will also contribute to tail states [72,73].

The Urbach energy is determined from the exponential behaviour of the absorption coefficient below the band gap. For an accurate determination of the Urbach energy the measurement of very low absorption coefficients is necessary [74,75]. Since in general it is easier to detect single emitted photons than to detect missing photons, photoluminescence (PL) is particularly suited to measure ultra-low absorption coefficients and thus allows a reliable determination of the Urbach energy [76,77].

It is been long known that tail states contribute to a radiative loss in open circuit voltage [78]. In that work, tail states were described as a Gaussian variation of the band gap, which is not exactly the same as an Urbach tail, but qualitatively the arguments also hold for Urbach tails: the main reason for the radiative V_{OC} loss is the fact that the carriers can thermalise to lower energy states in the case of tails. An expansion of this model is presented in ref. [79], where the open circuit voltage losses are discussed based on detailed balance, using an arbitrary shape of the quantum efficiency spectrum that can include any shape of tail states. Since alkali postdeposition treatments (see sect. 5) allow to manipulate the Urbach energy [73], the influence of these states on the V_{OC} loss can be investigated experimentally [62]. Figure 3 shows a number of different Cu(In,Ga)Se$_2$ solar cells, together with various cells from the literature ([62] and references therein). It is evident that every additional meV in the Urbach energy increases the V_{OC} loss by 20 mV. Several experimental parameters influence the Urbach energy: higher process temperature leads to lower Urbach energy (compare the samples labeled "H" with those labelled "L"); also treatment with heavy alkalis, like Rb decreases the
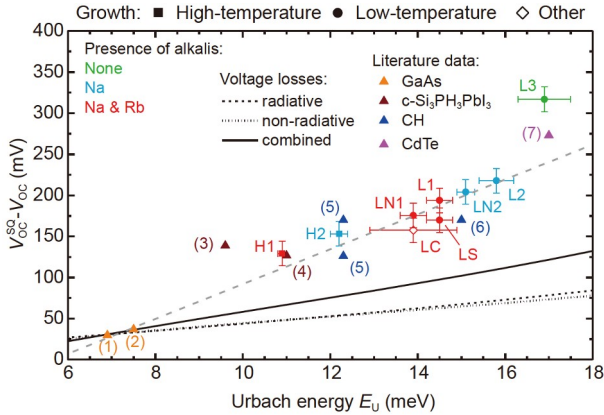
Figure 3 (Color online) V_{OC} loss with respect to the Shockley-Queisser V_{OC} according to the bandgap of the respective cells, as a function of the Urbach energy of the tail states. Every increase in the Urbach energy of 1 meV leads to an additional V_{OC} loss of 20 mV. We compare a range of different Cu(In,Ga)Se$_2$ solar cells with various other cells from the literature. Shown is also the theoretical radiative and the non-radiative loss due to tail states, assuming everything else remains unchanged. From ref. [62] (reproduced under CCBY licence).

Urbach energy (compare samples labelled "1" with those labelled "2"). Based on the Urbach energy alone it is possible to calculate the loss in V_{OC} due to radiative recombination (thermalisation into tails states) and due to non-radiative recombination (Shockley-Read-Hall recombination through tail states), also shown in Figure 3. The actual loss increases stronger than the combined effect of those two losses. The reason is most likely that additional effects in doping occur: lower doping would reduce V_{OC} and increase electrostatic potential fluctuations simultaneously. This explanation is supported by the observation that alkali addition increases the doping level and reduces the Urbach energy (see sect. 5).

It should be mentioned that the Urbach energies measured in Figure 3 are from tail states deep in the gap. A distribution of bandgaps has similar effects [78,79], but would be observed near the effective band gap [80,81]. State-of-the-art chalcopyrite solar cells certainly suffer from a distribution of band gaps, visible in the broadening of the onset of absorptance [82] or the quantum efficiency [79], which is due to the intentionally graded band gap. The effects of tail states and band gap distribution are linked and difficult to disentangle experimentally.

No deep defects were found in the absorbers shown in Figure 3 [83]. For a given Urbach energy of the absorber, the V_{OC} loss can be higher than the dashed line in Figure 3, if additional deep defects or recombination channels at the interfaces exist. However, the loss cannot be lower than the one dictated by the Urbach energy. It can, thus, be summarized that the open circuit voltage of state-of-the-art chalcopyrite solar cells is limited by the effects of tail states or band gap distribution.

5   Alkali addition: doping and interface modification

Na is the first alkali metal, which was identified to increase the efficiency of CIGS solar cells. The beneficial effect of Na was discovered, where Na was introduced unintentionally into the CIGS growth process by using soda-lime-glass substrates [13]. Generally, average concentrations of approximately 0.1 at.% are found to be optimal [84], while too much Na deteriorates the performance [85].

The main benefit of the addition of Na is an increase in net doping density of the CIGS absorber layer. While the net p-type doping of the alkali-free Cu-poor absorber is only on the order of 10^{14} cm^{-3}, it increases by up to 2 orders of magnitude upon the addition of Na [86,87]. Importantly, the increase in the doping describes well the increase of the open-circuit voltage [86-88], which is the main reason for the improved performance. Often, an increase in the FF is reported as well, which is however expected due to an increased V_{OC}. Additional improvements of the FF might be caused by a reduced series resistance due to the increased net p-type doping or a reduced diode factor. Unfortunately, these contributions are generally not disentangled.

The microscopic origin for the increased p-type doping is still under debate. Kronik et al. [89] suggested that Na catalyses the passivation of donor-like Se-vacancies by O. This model is supported by the correlation of Na and O in the near surface region of the CIGS absorber as well as the formation of In–O bonds [84,88]. In addition, Abou-Ras [90] found segregation of Na, K, and O at random grain boundaries and speculated that O$_{Se}$ might act as an acceptor.

Another model assumes Na$_{In}$ and Na$_{Ga}$ acceptor-like point defects, which is based on the presence of Na–Se bonds by XPS, while metallic Na bonds (Na–Na, Na–Cu, Na–In and Na–Ga) could be excluded [84]. Contreras et al. [91] propose that Na inhibits the formation of In$_{Cu}$ and Ga$_{Cu}$ antisite donor-like defects and thus an increase in the net p-type doping due to reduced compensation.

More recently, Yuan et al. [92] proposed a new mechanism explaining the increased net p-type doping caused by Na. In their calculations, in contrast to previous approaches, the thermodynamic limiting condition to the elemental chemical potential of Na is taken into account. As a result, Na$_{Cu}$ is the defect with the lowest formation energy. While Na$_{Cu}$ is a neutral defect, the increase in the p-type conductivity is explained by out-diffusion of Na (from Cu-sites) when cooling down the CIGS absorber. The driving force is a lower solubility of Na in the CIGS crystal at room temperature compared to elevated temperatures (growth temperature or PDT temperature). As a result, an increased density of V_{Cu} form in the CIGS bulk, which are shallow acceptors (see Figure 1 and Table 1).

Apart from an increase of the net-doping, Na influences

the growth of the CIGS absorber layers resulting in increased grain size [91] and preferred ⟨112⟩ texture [93]. Also the GGI grading, important to achieve high-efficiency absorbers, is influenced by the presence of Na [94,95], which however is different for polycrystalline and epitaxial films: it appears that Na supports the intragrain interdiffusion of In and Ga, whereas it hampers the intergrain diffusion. The latter effect was used, for example, by Zahedi-Azad et al. [96] who used substrates with a diffusion barrier to reduce the Na concentration during the growth of wide bandgap (high Ga) absorbers to smoothen the Ga grading and increase the efficiency.

Apart from Na, heavier alkalis are introduced into the growth process of CIGS absorber layers and are important to reach state-of-the-art quality. Already in 1997, Contreras et al. [91] used thin precursor layers of MF (M = Na, K, Cs) prior to the CIGS growth to investigate the influence of some other (heavier) alkalis. However, no additional beneficial effect was observed using heavier alkalis. Also, the highest increase in doping resulted from using a NaF precursor. Only in 2013, Chirilă et al. [97] introduced potassium as a KF post-deposition treatment (PDT), i.e., after the growth of the CIGS absorber layer. A record efficiency of 20.4% was achieved, followed by a series of record efficiencies by other institutes and companies [98]. One of the benefits of the KF PDT is that it enabled the reduction of the CdS buffer layer thickness and hence reduced parasitic absorption losses. Moreover, an increased V_{OC} was observed, which in this case exceeded the expected increase due to the doping density, thus suggesting another beneficial effect [86,99,100]. Chemically, the KF resulted in a Cu and Ga depletion and a K enrichment at the front surface [97]. It was then suggested by several studies that a K-In-Se layer forms at the front surface [101-103]. Lepetit [104] also suggested that this surface layer reacts during the CBD CdS deposition to form a $CdIn_2S_4$ layer. In any case, an increased diffusion of Cd into the Cu depleted surface was proposed as a reason for the improved V_{OC} [86]. The model is based on Cd_{Cu} donor defects, which help to increase the surface inversion and thereby prevent interface recombination [27]. It is likely that these defects form in any case, but they form faster in the Cu-depleted layer, which is obtained after the PDT, allowing for a shorter CdS deposition time and thinner buffer layer. It was also shown that a PDT by RbF acts very similar to a KF PDT [105], and a Rb-In-Se phase, identified as a $RbInSe_2$ structure, was directly observed by TEM analysis [106]. The formation of the $RbInSe_2$ phase was found to depend on the Cu content of the absorber and on the availability of Cu vacancies to be occupied by Rb [107]. An overtreatment was found to hamper the fill factor [108,109], which is attributed to the formation of a barrier because of the wide bandgap of the $RbInSe_2$ layer [110].

Several authors have suggested that the V_{OC} improvement

was due to reduced surface recombination. This reduced surface recombination was partly attributed to the observed widening of the surface band gap [111] which can be caused by a $KInSe_2$ or an $RbInSe_2$ layer at the surface, which have wide band gaps. However, a wider surface band gap is generally observed in Cu-poor $Cu(In,Ga)Se_2$ [112,113]. A reduced surface recombination was also concluded based on the temperature and generation dependent V_{OC} measurements [100,114], according to the model of ref. [115]. However, the model proposed in ref. [115] depends on assumptions that are not correct: e.g., the hole barrier at the front interface (i.e., distance of the Fermi level to the valence band) is interpreted as activation energy of the reverse saturation current in case of interface recombination. However, this is not the case as the hole barrier itself is temperature dependent [116,117]. Furthermore, standard Cu-poor devices without alkali PDT are not limited by interface recombination [27,69]. It is therefore highly unlikely that the observed V_{OC} improvement should be due to interface recombination.

Recently, based on the effort of a large consortium, it was concluded that the heavy alkali treatment has a strong beneficial effect on the absorber bulk properties [38,73]. First, the addition of heavy alkalis reduced disorder in the CIGS bulk material, as evidenced by reduced Urbach tails [62,73], which are shown to correlate well with the V_{OC} losses [61,62]. Second, reduced variations of potential fluctuations at grain boundaries are found [118]. In particular, for RbF (for which the process was optimized), only an upward band bending was found, i.e., electrons (minorities) are repelled from the GBs. Thus, GB recombination is reduced. The main findings are summarized in Figure 4.

This finding is in agreement with the results from Krause et al. [119], who recently reported that grain boundary recombination contributes significantly to V_{OC} losses in state-of-the-art CIGS absorbers. Alkalis tend to segregate at GBs [120], in particular the heavy alkalis are almost exclusively found at the grain boundaries [73]. This trend can be explained by the thermodynamics of the segregation of Alkali-In-Se compounds versus the formation of mixed (Cu-Alkali)-In-Se compounds. Heavy alkalis (K, Rb, Cs) segregate at growth conditions, whereas Na and Li form mixed compounds [110]. Although it was shown that alkali accumula-
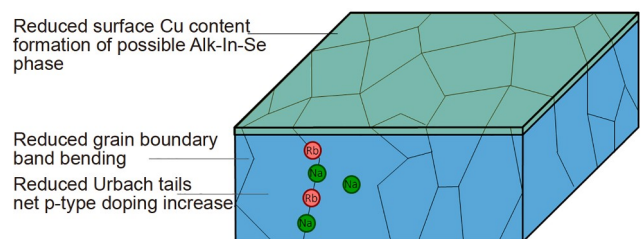
Figure 4 (Color online) Summary of effects due to alkali doping and heavy-alkali post-deposition treatment.

tion does not reduce the recombination velocity at grain boundaries [121], it is likely that alkalis change the charge state of defects at grain boundaries and thus the band bending around them, which will influence tail states and the effective grain boundary recombination [73]. On the other hand, KF postdeposition treatment was also found to increase the quasi-Fermi level splitting in single crystalline films [122]. And similar reductions of the Urbach tails were observed in single crystalline films upon alkali postdeposition treatment as in polycrystalline films [123]. Both effects indicate that the improvement goes beyond grain boundary effects.

6   Ag compounds

The addition of Ag to form $(Ag,Cu)(In,Ga)Se_2$ (ACIGS) absorbers enables another handle to modify the electronic structure of the CIGS absorber as well as the growth process. Avon et al. [124] showed that the $Ag(In,Ga)Se_2$ and $Cu(In,Ga)Se_2$ compounds are not entirely miscible over the whole Ag-Cu compositional range, based on samples grown in sealed quartz ampules at temperatures between 600°C and 800°C. However, growth of thin-films by co-evaporation showed complete miscibility, i.e., the entire compositional space of $(Ag,Cu)(In,Ga)Se_2$ results in single-phase material (i.e., possible secondary phases are below detection limit of X-ray diffractometry (XRD)) [125-128]. Sopiha et al. [129] studied the phase diagram theoretically based on density functional theory (DFT) calculations and experimentally by glow discharge optical emission spectroscopy (GDOES) and by transmission electron microscopy (TEM). The authors showed that spinodal and binodal decomposition of the ACIGS absorber can occur for most Ga/(Ga+In) and Ag/(Ag+Cu) atomic ratios at room temperature. At 350°C (typical PDT temperatures), the decomposition may only occur for Ga/(Ga+In) ratios > 0.4, conditions, which however are found towards the back contact in graded (A)CIGS absorbers. However, it seems that the kinetics are rather slow at room temperature, which explains the single-phase thin-film materials mentioned above [125-128]. It is noted that some decomposition at the front surface is observed under certain process conditions (overall high Se flux and high substrate temperature in the first stage of a 3-stage co-evaporation process) for films with Ag/(Ag+Cu) = 0.5 and Ga/(Ga+In) = 0.85 [126], which is the least stable region reported in ref. [129]. Keller et al. [130] find a significant formation of order vacancy compound (OVC) phases as the front and back contact for high Ag (Ag/(Ag+Cu) = 0.8) and high Ga (Ga/(Ga+In) = 0.72-0.85) absorbers. Also, degradation of finished solar cells after 8 month storage in air for samples with Ag/(Ag+Cu) = 0.8 and Ga/(Ga+In) = 0.72-0.85 is observed most likely linked to formation of ordered vacancy compounds (OVC) [130]. These features might be associated with the miscibility gap mentioned above [129]. This degradation did not happen for samples with AAC = 0.5 and the same GGIs, which is surprising as samples with AAC = 0.5 are calculated to have the highest free energy of mixing [129] and should therefore show a faster degradation/decomposition.

Another interesting prediction from the calculation of the total free energy of an ACIGS absorber is the anti-correlation of the Ag/(Ag+Cu) profile to the (fixed, because group-III diffusion is much slower) Ga/(Ga+In) profile [129], which is generally observed experimentally as well [126,129,131, 132].

Early studies reported a very similar 3-stage deposition process for ACIGS [126], as it was applied for high-efficiency $Cu(In,Ga)Se_2$ [14]. In particular, a Ga notch forms, i.e., the Ga concentration is graded and increases towards the front and back surfaces [126,132,133]. However, Essig et al. [133] performed interruption process, where the ACIGS absorbers grown on glass/Mo substrates are taken out during the 3rd stage, where the composition is stoichiometric and/or (Ag,Cu)-poor again. It is found that Ag-rich islands form for (Ag+Cu)/(Ga+In) atomic ratios greater >0.9. It is speculated that these islands are a result of a faster reaction of Cu with the $(In,Ga)_2Se_3$ layer deposited in the 1st stage [133,134]. Also Valdes et al. [135] observes a Ag-rich surface for (Ag,Cu)InSe_2 absorbers. For compositions with (Ag+Cu)/(Ga+In) < 0.9, local variations in the Ag/(Ag+Cu) and Ga/(Ga+In) ratio are still observed [133], probably caused due to similar reasons as the Ga and Ag anti-correlation mentioned above, which are expected to be detrimental to device performance [129]. Another consequence of the Ag-rich islands is that the surface shows an increase of the Ag content, i.e., the anti-correlation of the Ga/(Ga+In) and Ag/(Ag+Cu) is not maintained in that region. This is in stark contrast to the observations of Edoff et al. [136], who showed a strong group I depletion with thicknesses ranging from 50 to 300 nm at the front surface. At the same time, a K enrichment is observed within this front surface layer. Noteworthy, this group I depletion and K enrichment was only observed when using a high strainpoint glass having a high concentration of K and a low concentration of Na. No such surface layer was found when using SLG. Further studies are needed to clarify the role of alkalis on the group-I depleted surfaces in ACIGS absorbers, as it might help to reduce inhomogeneities of Ag/(Ag+Cu) and Ga/(Ga+In).

An important property of the Ag alloying is that it lowers the melting point [11] of the chalcopyrite compound. Consequently, enlarged grains are generally observed for absorber layers with increasing Ag content or when compared to Ag free absorbers grown under the same process conditions [132,133]. For instance, Essig et al. [133] found grain sizes >10 μm for ACIGS absorbers with Ag/(Ag+Cu) = 0.2 grown at a maximum temperature of 650°C, while crevices form at the same time, which can lead to shunt paths. Also, the

growth temperature can be reduced, without a sacrifice in device performance when adding Ag to the CIGS growth process [137].

Apart from the thermodynamic properties, which influence the growth of ACIGS absorbers, opto-electronic properties are strongly influenced by Ag-alloying. In particular, the bandgap is increased upon Ag alloying, which was experimentally determined by transmission and reflection measurements [127,138], however, the two studies find somewhat different bandgap values for high Ag and high Ga values. These discrepancies are probably caused due to the non-linear behaviour in the Tauc plots ($(\alpha E)^2$ versus E) and thus the derived bandgap values depend on the choice of the fitting region. Bandgap values are also reported based on DFT calculations, where it was shown additionally that the increase in the bandgap is caused by a downshift of the valence- and conduction-band [131]. This phenomenon is unlike Ga alloying to $CuInSe_2$, where mainly the conduction band shifts upward [139]. A comparison of various band alignments in the chalcopyrite system is shown in Figure 5 [131,139]. The implications for this modification of the band alignment with ACIGS absorbers are discussed below.

The early work of Ag alloying to CIGS focused on high bandgap, i.e., high Ga, absorber layers. The first high-bandgap ($E_g = 1.70$ eV) $Ag(In,Ga)Se_2$ solar cell was reported by Nakada et al. [140] in 2005 with an efficiency of 9.3% and a V_{OC} of 0.949 V. Shafarman et al. [128] showed that Ag allows to increase the bandgap, without losses in efficiency, i.e., beyond the threshold of $E_g = 1.25$ eV, which is associated with larger V_{OC} losses [141]. Erslev et al. [142] find that the addition of Ag results in Urbach energies (determined in both contributions by transient photocapacitance spectroscopy) between 10 and 15 meV, which are significantly reduced compared to CIGS absorbers with Urbach energies between 18 and 26 meV at that time [143]. The authors attribute the reduced Urbach energies due to a reduction of structural defects due to the lower melting point upon Ag alloying. The decrease of the Urbach energy with the addition of Ag is an important finding, due to the correlation of the V_{OC} loss, as discussed in sect. 4. Keller et al. [131] used Ag alloying in order to modify the conduction band offset at the front interface. In particular, due to the downshift of the conduction

band with increasing Ag concentration, the interface with CdS (or another buffer layer) can be changed from a "cliff" to a "spike"-like band alignment [131]. While Ag alloying allows to engineer the interface quality and thus reduce front surface recombination, recent studies suggest that absorbers with high Ga contents (GGI > 0.5) still suffer from a lower bulk quality, as for instance evidenced in ref. [144] by a small diffusion length of minority carriers (electrons). Thus, the reason for a V_{OC} saturation when increasing the bandgap of the absorber by increasing the Ga concentration seems not be solved when alloying additionally Ag. However, further defect studies are needed to draw more substantiated conclusions.

Recently, Ag is added/alloyed to low Ga CIGS (i.e., low bandgap around 1.0 to approximately 1.25 eV) as well due to the properties mentioned above. Edoff et al. [136] demonstrated that the mean voltage loss with respect to the bandgap is decreased for ACIGS devices (449 mV) compared with CIGS devices (460 mV), which is mentioned to be significant, where the bandgap for the ACIGS devices is approximately 50 meV higher (around 1.22 eV). This characteristic might be beneficial for modules, due to a lower current density, which then requires a thinner TCO. Finally, a champion device with a 20.9% power conversion efficiency, a V_{OC} of 814 mV with a bandgap of 1.22 eV is achieved (with Ag/(Ag+Cu) = 0.2 and Ga/(Ga+In) = 0.4) [136]. Essig et al. [133] achieved a 20.5% efficient device with Ag/(Ag+Cu) = 0.05 and Ga/(Ga+In) = 0.3. Yang et al. [137] used a 15 nm Ag precursor layer prior to a low temperature CIGS growth process [137]. Significantly higher efficiencies than without Ag are obtained when lowering the substrate temperature. In particular, efficiencies of 19.6% and 18.5% are demonstrated for substrate temperatures of 353°C and 303°C [137]. Also, similar as for high Ga containing absorbers [142], lower Urbach energies are measured for these samples with the Ag precursor layer [137].

Another important electronic modification is the doping density, which often is reported to be lower upon Ag alloying. In 2009, Erslev et al. [142] reported a very low carrier concentration on the order of 10^{14} cm^{-3} for Ag-alloyed absorbers, even though they are grown on SLG at a growth temperature of 550°C, in agreement with an improved carrier collection due to enlarged space charge region widths [125]. However, a later study showed a smaller difference of carrier concentrations between rather high efficient CIGS and ACIGS devices, where ACIGS devices have free carrier densities around 2×10^{15} cm^{-3} as measured by Drive Level Capacitance Profiling (DLCP) [145]. The authors speculated that the increased carrier densities results from a decrease in contamination during the growth process. Valdes et al. [146] found a reduced carrier concentration for ACIS compared to CIS (i.e., absorbers without Ga). For low temperature grown CIGS (substrate temperatures between 350°C and 410°C)
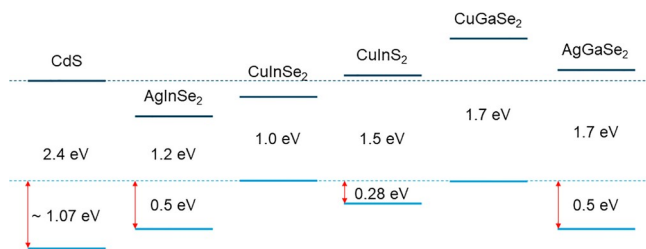
Figure 5 (Color online) Band alignments between different chalcopyrites and the most used buffer CdS. Data taken from refs. [131,139].

and the addition of Ag via a precursor layer, Yang et al. [137] observed also a lower apparent doping density for ACIGS than for CIGS. On the other hand, Kim et al. [147] found an increase in carrier density when using Ag precursor layers for low temperature (450°C) (A)CIGS absorbers. Keller et al. [144] demonstrated that the doping density depends on the stoichiometry of the absorber, i.e., the group-I over group-III ratio for rather large bandgap ACIGS absorbers (Ag/(Ag+Cu) = 0.53, Ga/(Ga+In) = 0.66). Interestingly, the doping density decreases the closer the absorber shifts towards the 1:1:2 stoichiometry point [144], which is in contrast to the observations for Ag-free CIGS absorbers [69]. If these results also hold for lower bandgap ACIGS devices, variations in the stoichiometry could explain the different results.

The importance of the doping density is that it has a direct impact on the V_{OC}. An improvement/deterioration of the V_{OC} by 60 mV can be expected for an increase/decrease of the doping density by 1 order of magnitude [59]. Valdes et al. [146] investigated low bandgap (1.0 eV) (Ag,Cu)InSe$_2$ based solar cells with and without Ag alloy. In this study, the ACIS solar cells had a reduced V_{OC} of approximately 30 mV, which could be attributed to the decrease of the doping density. In particular, for low Ag contents (Ag/(Ag+Cu) < 0.25), no increase in the bandgap is expected for (Ag,Cu)InSe$_2$ absorbers [131], which facilities in this case the analysis. However, for samples including significant amounts of Ga and Ag, a detailed detanglement of the different contributions to V_{OC} due to bandgap and doping density is missing. Nevertheless, Edoff et al. [136] stated that a comparison of various ACIGS and CIGS samples with the comparable bandgap indicated a small performance advantage for ACIGS. Unfortunately, measurements of the doping density were missing to judge the quality of the ACIGS material better.

Interestingly, some studies show large fill factors for ACIGS devices [60,128,133]. It is stressed that FF values are not always comparable between various samples with significant different V_{OC} values, because of the dependence of FF on V_{OC} [60]. A more suitable parameter for comparison is the diode factor of the solar cell, which is the main parameter governing the FF, assuming that the solar cell does not suffer from too large series ($> 0.4 \, \Omega \, cm^2$) or too low shunt ($< 1 \, k\Omega \, cm^2$) resistances [60]. Unfortunately, this parameter is not always determined for the published IV characteristics. Shafarman et al. [128] reported a diode factor of 1.1 for the device with the highest FF, which the authors attributed to improved carrier collection. Also Edoff et al. [136] reported that ACIGS devices generally have a lower diode factor compared with CIGS devices, whereas the diode factors are still rather large around 1.4 for their record device. Valdes et al. [135] reported a higher FF for low bandgap (1.04 eV) ACIGS compared to CIGS (also E_g = 1.04 eV), even though

the V_{OC} shows the opposite trend, which indicates an improvement in the diode factor. It is noted however, that their CuInSe$_2$ and (Ag,Cu)InSe$_2$ devices show an opposite trend, higher V_{OC} with Ag, but lower FF. Diode factors greater than 1 are often associated with contributing SCR recombination as diode factors close to 2 are expected for this recombination channel [59]. However, the diode factor can also be measured optically on the bare absorber, i.e., without SCR, by intensity dependent photoluminescence spectroscopy [57,58,148], often labeled optical diode factor (see also sect. 3). It is found that for CIGS absorbers the optical diode factor is already greater than 1 for these measurements, where no SCR is present, and with commonly reported values around 1.3 [56,58]. Weiss et al. [56] showed that metastable defects, such as the V_{Se}-V_{Cu}, can explain an increase in the diode factor. The metastable defects change from a donor-type to an acceptor-type defect upon injection of minority carriers (electrons). Thus, the diode current is altered during a voltage sweep, which results in increased diode factors. Interestingly, upon alloying CIGS with Ag, the smallest optical diode factors (around 1.1) as well as electrical diode factors (around 1.14 obtained from IV characteristics) are obtained [60]. In addition, it is demonstrated that this Ag-alloyed samples shows much weaker metastability as detected by capacitance based methods [60].

In conclusion, it seems promising that Ag alloying may contribute to the success of the CIGS thin-film photovoltaic technology. It reduces the Urbach energy and allows to fabricate higher bandgaps high efficiency CIGS devices. In addition, due to the lowered melting point, the growth process may be modified such that a faster deposition or lowered temperature can be implemented without a sacrifice in efficiency and thus might be particularly important for industry. However, there are still open questions, such as the impact on the doping density, including metastable defects, and its influence on the V_{OC} and FF.

7   Back contact passivation

In any solar cell the (necessary) metal back contact leads to high recombination. State-of-the-art PERC Si solar cells are, therefore, equipped with a dielectric layer between the absorber and the back contact with small holes to let the current pass [149]. The standard way for backside passivation in chalcopyrite solar cells is a Ga gradient, which results in a gradient of the conduction band edge that prevents the electrons from reaching the highly recombinative back contact [14,15]. A sketch of both approaches is shown in Figure 6. We have recently shown quantitatively that a Ga gradient reduces the backside recombination as effectively as a dielectric layer [150]: both increase the quasi-Fermi level splitting by almost 50 meV for a mediocre absorber with a
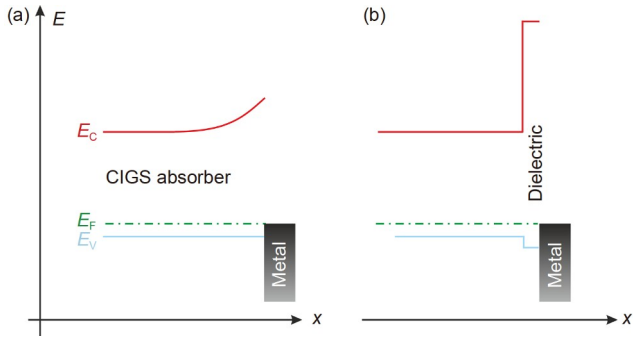
Figure 6 (Color online) Band diagram schematics of back contact passivation. (a) Ga gradient that reduces electron concentration at (highly recombinative) metal back contact; (b) dielectric layer that is either thin enough to allow tunnelling of holes or is structured to open pathways for the current or a wide gap semiconductor with sufficient hole conductivity.

bulk lifetime of 40 ns. In a good absorber with a lifetime of 200 ns [151] the improvement increases to 80 meV [150]. These experiments and simulations were performed with rather thick absorbers of 3 μm thickness. In contrast to some studies in the literature we find that even at this thickness back contact recombination does have a significant influence.

However, it is desirable to decrease absorber thickness, to reduce production cost and in particular reduce the consumption of costly and rare indium. Although it was recently shown that accessible In resources are 35 times higher than previously assumed [152]. First experiments to reduce absorber thickness were already performed 20 years ago [153]. Various light management techniques have been used to improve the absorption in thin Cu(In,Ga)Se$_2$ layers, including plasmonic structures and improved back reflectors, see e.g., refs. [154-159]. With decreased absorber thickness back contact recombination becomes ever more important. Thus the concept of the PERC solar cell has been transferred to Cu(In,Ga)Se$_2$ solar cells: dielectric layer passivation at the back contact with point contact openings to let the current pass [160]. The challenge compared to Si solar cells is the shorter diffusion length in chalcopyrite solar cells, which requires a much denser grid of contact holes [160]. Various dielectrics have been successfully used as passivating layers at the back contact: Al$_2$O$_3$ [160], SiO$_2$ [161], TiO$_2$ [162]. Patterning methods range from arbitrarily distributed nanoparticles [160] through nano-imprint lithography [162] and laser interference lithography [161] to e-beam lithography [163]. A review can be found in ref. [164]. In general an improvement of the open-circuit voltage is observed with a passivated back contact; the difference increases with decreasing thickness [164]. This is expected since the recombination at the back contact is reduced. An increase in the short circuit current is also observed in many cases [164] which can be attributed to optical effects [161].

While the approach of a structured dielectric layer to passivate the back contact has been successful, it might be

difficult to scale up to industrial scales. Another approach to a passivated back contact is to use ultrathin dielectric layers, which can be tunnelled through or are conductive enough, not to block the current. A 3 nm thick TiO$_2$ layer has been shown to effectively reduce backside recombination and to lead to a considerable increase of V_{OC} and j_{SC} for a 1 μm thick Cu(In,Ga)Se$_2$ absorber without backside gradient [165]. We believe that more work is needed on continuous dielectrics or wide gap semiconductors that can serve as selective hole contact at the back side and reduce recombination at the back contact.

8   Tandem cells and wide bandgap chalcopyrites

While single junction chalcopyrite solar cells can still be improved, e.g., with a new device design [19,20], much higher efficiencies can be expected with tandem solar cells [166,167]. For the schematics of the loss mechanisms in single and tandem solar cells see Figure 7. Low bandgap Cu(InGa)Se$_2$ has been combined with perovskite solar cells, to reach efficiencies above 26% [168-171]. Monolithic 2-terminal, as well as stacked 4-terminal architectures have been used. One challenge for the monolithic tandem is the rather rough surface of the Cu(In,Ga)Se$_2$ bottom solar cells. Using optimised Cu(In,Ga)Se$_2$ processing and solution based deposition of the perovskite solar cell, this problem has been overcome [169]. Interestingly, a comparatively simple self-assembled monolayer on top of the TCO contact of the Cu(In,Ga)Se$_2$ cell acts as a tunnel junction between the two devices [169] A certified efficiency of 24.2% has been achieved [169]. Since no procedure exists yet to certify stacked tandem cells, only in-house measurements are
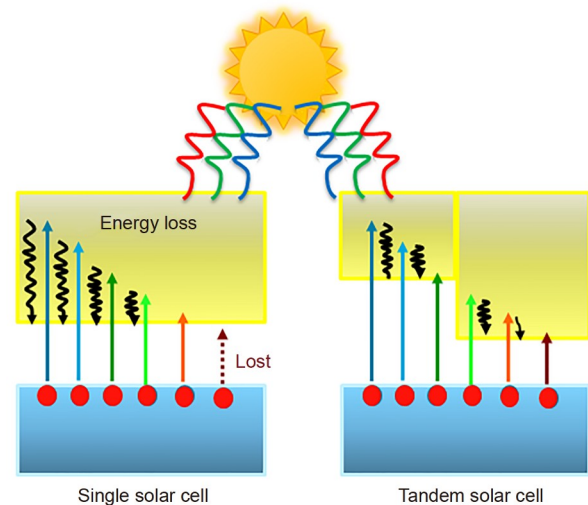
Figure 7 (Color online) Main losses in single junction solar cells: insufficient absorption and thermalisation. With a lower band gap bottom cell more photons can be absorbed and the higher band gap top cell reduces the thermalisation losses in both cells.

available. The highest reported efficiency is 26.2%, based on a highly efficient Cu(In,Ga)(S,Se)$_2$ solar cell in combination with an improved transparent perovskite solar cell [171]. Recently, a triple junction with 28% efficiency was obtained, combining a InGaP/AlGaAs tandem with a Cu(InGa)Se$_2$ bottom cell [172]. Considerable progress has been made recently improving low band gap Cu(In,Ga)Se$_2$ solar cells to 19.2% efficiency [173].

Another approach is to use widegap chalcopyrite in combination with a Si bottom cell or a low bandgap Cu(In,Ga)Se$_2$ cell [174]. This approach requires obviously highly efficient, transparent wide gap chalcopyrite solar cells. So far, most wide gap chalcopyrites solar cells have been optimised on a Mo back contact, thus, they can only be considered a first step towards a top cell in a tandem device. However, some promising improvements in the efficiency have been reported recently. In general, wide gap semiconductors can be expected to have a higher V_{OC} loss because of increased non-radiative recombination due to an increasing number of different deep defects. More deep defect levels are in fact found in widegap Cu(In,Ga)(S,Se)$_2$ (see sect. 3) [39].

The targeted bandgap for top cells is around 1.5 to 1.7 eV. In fact, it was recently shown that in combination with a realistic bifacial Si solar cell a top cell band gap of 1.5 eV can be sufficient [175]. Several options exist to achieve wide gap chalcopyrites: high Ga Cu(In,Ga)Se$_2$ or pure CuGaSe$_2$, alloying with S or pure sulfide Cu(In,Ga)S$_2$, or alloying with Ag (Ag,Cu)(In,Ga)Se$_2$. For the latter see sect. 6. An overview of current best published efficiencies of wide gap chalcopyrites is given in Table 2 [131,176-180]. As becomes obvious from the table, all wide gap chalcopyrites, besides CuGaSe$_2$, reach efficiencies around 15%. This is about the critical efficiency for a top cell in a tandem solar cell [181,182].

Obviously further improvements are necessary, so it is worth having a look at current limitations. As mentioned above: in general wide gap semiconductors are more prone to non-radiative recombination because they host more deep defect levels [39]. Another issue is the interface between the absorber and the buffer. With increasing Ga or S the conduction band shifts upwards [139]. Therefore, above a certain Ga or S content the absorber conduction band edge will be above the buffer conduction band edge, forming a cliff, which increases interface recombination [59], in particular when using the standard CdS buffer. In general, alternative buffer layers are necessary to avoid this interface recombination. Examples are Zn(S,O) [178], (Zn,Mg)O [177,183], (Zn,Sn)O [184]. However, the alternative buffer layers lead to a large cliff towards the standard i-ZnO layer, which limits the forward current and thus the fill factor [183]. A high resistive i-layer is generally necessary to avoid the influence of inhomogeneities and local diodes with a low V_{OC} [185]. An i-layer with a higher conduction band edge, like

Table 2 Best reported efficiencies of wide gap chalcopyrite solar cells

Absorber material	Band gap (eV)	Efficiency (%)	Reference
(Ag,Cu)(In,Ga)Se$_2$	1.45	15.1	[131]
Cu(In,Ga)Se$_2$	1.50	14.2	[176]
Cu(In,Ga)S$_2$	1.50	15.5	[177]
Cu(In,Ga)S$_2$	1.60	15.2	[178]
CuGaSe$_2$	1.65	11.9	[179]
Cu(In,Ga)S$_2$	1.65	14.2	[180]

(Zn,Mg)O, can avoid this problem and lead to better fill factors [183]. As discussed in sect. 6, the situation is different for the Ag compounds: here both band edges shift downwards and CdS is still a useful buffer [131].

9 Outlook

State-of-the-art chalcopyrite solar cells are limited by bulk recombination due to tail states. Interface recombination does not play a role, because the front surface is passivated by the buffer layer [186] and the back surface is passivated by the Ga gradient. Efficient back side passivation has also been demonstrated by structured or continuous layers of various dielectrics.

The recent progress in efficiency has been made possible by alkali postdeposition treatments. The main effect of this treatment is a reduction of the non-radiative recombination in the bulk due to the reduction of tail states. Tail states are the main source of V_{OC} loss in state-of-the-art chalcopyrite solar cells.

Several recent reviews have called for a paradigm change [19,20] in the development of chalcopyrite cells: replacing the Ga gradient by a selective contact at the back. Dielectric layers can also passivate the back contact. An absorber without band gap grading would show a sharper absorption edge and thus less radiative and non-radiative V_{OC} loss due to tail states. However, without the Ga gradient new ways must be found to passivate the back contact. Much more research is needed on selective and passivated back contacts. The electrostatic contributions to tail states (doping compensation and charged grain boundaries) can be reduced by using absorbers with higher doping level. In general higher Cu content leads to higher net doping [39,69], thus it appears desirable to grow the chalcopyrite absorbers as close as possible to stoichiometry. It is necessary to maintain a Cu-poor composition, to avoid the problems of the Cu-rich surface [187,188]. The higher doping level will also be beneficial for the open circuit voltage.

The efficiency of state-of-the-art chalcopyrite cells is further limited by the rather high diode factor which leads to a low fill factor. Metastable defect transitions increase the diode factor. This implies another call for more research: to

find ways to suppress the metastable defects. Alloying with Ag appears beneficial in that context.

A massive increase in efficiency can only be expected from tandem cells. Chalcopyrite cell shows convincing potential as bottom cells as well as for top cells. It should be noted, though, that a recent economic study found, that tandem cells are certainly the preferred choice where the area is limited, e.g., on roofs, however, for utility scale project it might economically more attractive to use a highly efficient and low cost single junction cell [189,190]. Thus, it is certainly worthwhile to further improve the efficiency of single junction chalcopyrite solar cells.

We thank Marika Edoff, Roland Scheer and Wolfram Witte for many useful discussions and for their support in collecting some of the data, in particular Table 2.

1 F. Creutzig, P. Agoston, J. C. Goldschmidt, G. Luderer, G. Nemet, and R. C. Pietzcker, Nat. Energy **2**, 17140 (2017).

2 M. Ram, D. Bogadnov, A. Aghahosseini, A. S. Oyewo, A. Gulagi, M. Child, H.-J. Fell, and C. Breyer, *Global Energy System based on 100% Renewable Energy-Power Sector* (Lappeenranta University of Technology and Energy Watch Group, 2017).

3 E. G. Hertwich, J. Aloisi de Larderel, A. Arvesen, P. Bayer, J. Bergesen, E. Bouman, T. Gibon, G. Heath, C. Peña, P. Purohit, A. Ramirez, and S. Suh, eds., *Green Energy Choices: The Benefits, Risks and Trade-Offs of Low-Carbon Technologies for Electricity Production*, Report of the International Resource Panel, United Nations' Environment Programme, 2016.

4 A. Müller, L. Friedrich, C. Reichel, S. Herceg, M. Mittag, and D. H. Neuhaus, Sol. Energy Mater. Sol. Cells **230**, 111277 (2021).

5 S. Amarakoon, C. Vallet, M. A. Curran, P. Haldar, D. Metacarpa, D. Fobare, and J. Bell, Int. J. Life Cycle Assess **23**, 851 (2018).

6 B. Gao, Y. Shao, W. Liu, H. Xiang, Y. Yu, and Z. Liu, Sol. Energy Mater. Sol. Cells **236**, 111490 (2022).

7 J. Palm, L. Tautenhahn, J. Weick, R. Kalio, J. Kullmann, A. Heiland, S. Grünsteid, N. Schmidt, P. Borowski, and F. Karg, in *BIPV modules: Critical requirements and customization in manufacturing: Proceedings of the in 7th IEEE World Conference on Photovoltaic Energy Conversion (WCPEC)/A Joint Conference of 45th IEEE PVSC/28th PVSEC/34th EU PVSEC*, Waikoloa, 2018.

8 M. Powalla, S. Paetel, D. Hariskos, R. Wuerz, F. Kessler, P. Lechner, W. Wischmann, and T. M. Friedlmeier, Engineering **3**, 445 (2017).

9 B. H. King, J. S. Stein, D. Riley, C. B. Jones, and C. D. Robinson, in *Degradation assessment of fielded CIGS photovoltaic arrays: Proceedings of the in 2017 IEEE 44th Photovoltaic Specialist Conference (PVSC)*, Washington, 2017.

10 M. Nakamura, K. Yamaguchi, Y. Kimoto, Y. Yasaki, T. Kato, and H. Sugimoto, IEEE J. Photovol. **9**, 1863 (2019).

11 J. L. Shay, and J. H. Wernick, *Ternary Chalcopyrite Semiconductors: Growth, Electronic Properties, and Application*, In: International Series of Monographs in the Science of the Solid State, Vol. 7, edited by B. R. Pamplin (Pergamon Press, Oxford, 1975).

12 T. Wada, Jpn. J. Appl. Phys. **60**, 080101 (2021).

13 D. Abou-Ras, S. Wagner, B. J. Stanbery, H. W. Schock, R. Scheer, L. Stolt, S. Siebentritt, D. Lincot, C. Eberspacher, K. Kushiya, and A. N. Tiwari, Thin Solid Films **633**, 2 (2017).

14 A. M. Gabor, J. R. Tuttle, D. S. Albin, M. A. Contreras, R. Noufi, and A. M. Hermann, Appl. Phys. Lett. **65**, 198 (1994).

15 T. Dullweber, O. Lundberg, J. Malmström, M. Bodegård, L. Stolt, U. Rau, H. W. Schock, and J. H. Werner, Thin Solid Films **387**, 11 (2001).

16 A. Chirilă, S. Buecheler, F. Pianezzi, P. Bloesch, C. Gretener, A. R. Uhl, C. Fella, L. Kranz, J. Perrenoud, S. Seyrling, R. Verma, S. Nishiwaki, Y. E. Romanyuk, G. Bilger, and A. N. Tiwari, Nat. Mater. **10**, 857 (2011).

17 A. Rockett, Thin Solid Films **480-481**, 2 (2005).

18 D. Rudmann, D. Brémaud, H. Zogg, and A. N. Tiwari, J. Appl. Phys. **97**, 084903 (2005).

19 M. Ochoa, S. Buecheler, A. N. Tiwari, and R. Carron, Energy Environ. Sci. **13**, 2047 (2020).

20 B. J. Stanbery, D. Abou-Ras, A. Yamada, and L. Mansfield, J. Phys. D-Appl. Phys. **55**, 173001 (2021).

21 M. Powalla, S. Paetel, E. Ahlswede, R. Wuerz, C. D. Wessendorf, and T. Magorian Friedlmeier, Appl. Phys. Rev. **5**, 041602 (2018).

22 T. Feurer, P. Reinhard, E. Avancini, B. Bissig, J. Löckinger, P. Fuchs, R. Carron, T. P. Weiss, J. Perrenoud, S. Stutterheim, S. Buecheler, and A. N. Tiwari, Prog. Photovolt.-Res. Appl. **25**, 645 (2017).

23 S. Siebentritt, Curr. Opin. Green Sustain. Chem. **4**, 1 (2017).

24 V. Bermudez, and A. Perez-Rodriguez, Nat. Energy **3**, 466 (2018).

25 R. Carron, S. Nishiwaki, T. Feurer, R. Hertwig, E. Avancini, J. Löckinger, S. Yang, S. Buecheler, and A. N. Tiwari, Adv. Energy Mater. **9**, 1900408 (2019).

26 J. Ramanujam, D. M. Bishop, T. K. Todorov, O. Gunawan, J. Rath, R. Nekovei, E. Artegiani, and A. Romeo, Prog. Mater. Sci. **110**, 100619 (2020).

27 R. Klenk, Thin Solid Films **387**, 135 (2001).

28 C. Spindler, F. Babbe, M. H. Wolter, F. Ehré, K. Santhosh, P. Hilgert, F. Werner, and S. Siebentritt, Phys. Rev. Mater. **3**, 090302 (2019).

29 A. Gerhard, W. Harneit, S. Brehme, A. Bauknecht, U. Fiedeler, M. C. Lux-Steiner, and S. Siebentritt, Thin Solid Films **387**, 67 (2001).

30 Y. Aida, V. Depredurand, J. K. Larsen, H. Arai, D. Tanaka, M. Kurihara, and S. Siebentritt, Prog. Photovolt.-Res. Appl. **23**, 754 (2015).

31 A. Jasenek, U. Rau, V. Nadenau, and H. W. Schock, J. Appl. Phys. **87**, 594 (2000).

32 A. Bauknecht, S. Siebentritt, J. Albert, and M. C. Lux-Steiner, J. Appl. Phys. **89**, 4391 (2001).

33 S. Siebentritt, N. Rega, A. Zajogin, and M. C. Lux-Steiner, Phys. Stat. Sol. (c) **1**, 2304 (2004).

34 C. Stephan, S. Schorr, M. Tovar, and H. W. Schock, Appl. Phys. Lett. **98**, 091906 (2011).

35 S. Siebentritt, Thin Solid Films **403-404**, 1 (2002).

36 F. Werner, D. Colombara, M. Melchiorre, N. Valle, B. El Adib, C. Spindler, and S. Siebentritt, J. Appl. Phys. **119**, 173103 (2016).

37 O. Ramírez, E. M. Lanzoni, R. G. Poeira, T. P. Weiss, R. Leturcq, A. Redinger, and S. Siebentritt, APL Mater. **10**, 061108 (2022).

38 S. Siebentritt, T. P. Weiss, M. Sood, M. H. Wolter, A. Lomuscio, and O. Ramirez, J. Phys. Mater. **4**, 042010 (2021).

39 S. Siebentritt, A. Lomuscio, D. Adeleye, M. Sood, and A. Dwivedi, Phys. Rapid Res. Ltrs **16**, 2200126 (2022).

40 M. N. Ruberto, and A. Rothwarf, J. Appl. Phys. **61**, 4662 (1987).

41 N. Naghavi, S. Temgoua, T. Hildebrandt, J. F. Guillemoles, and D. Lincot, Prog. Photovolt.-Res. Appl. **23**, 1820 (2015).

42 J. Serhan, Z. Djebbour, W. Favre, A. Migan-Dubois, A. Darga, D. Mencaraglia, N. Naghavi, G. Renou, J. F. Guillemoles, and D. Lin-

cot, Thin Solid Films **519**, 7606 (2011).

43 I. Repins, S. Glynn, K. Bowers, B. Stevens, C. L. Perkins, and L. Mansfield, Sol. Energy Mater. Sol. Cells **215**, 110597 (2020).

44 I. Repins, S. Glynn, T. J. Silverman, R. Garris, K. Bowers, B. Stevens, and L. Mansfield, Prog. Photovolt.-Res. Appl. **27**, 749 (2019).

45 S. Siebentritt, M. Igalson, C. Persson, and S. Lany, Prog. Photovolt-Res. Appl. **18**, 390 (2010).

46 U. Rau, M. Schmitt, J. Parisi, W. Riedl, and F. Karg, Appl. Phys. Lett. **73**, 223 (1998).

47 M. Igalson, and H. W. Schock, J. Appl. Phys. **80**, 5765 (1996).

48 U. Rau, K. Weinert, Q. Nguyen, M. Mamor, G. Hanna, A. Jasenek, and H. W. Schock, MRS Proc. **668**, H9.1 (2001).

49 S. Lany, and A. Zunger, Phys. Rev. B **72**, 035215 (2005).

50 S. Lany, and A. Zunger, J. Appl. Phys. **100**, 113725 (2006).

51 A. Czudek, A. Urbaniak, A. Eslam, R. Wuerz, and M. Igalson, IEEE J. Photovol. **10**, 1926 (2020).

52 A. Czudek, A. Urbaniak, A. Eslam, R. Wuerz, and M. Igalson, Phys. Rapid Res. Ltrs **16**, 2100459 (2022).

53 S. Lany, and A. Zunger, Phys. Rev. Lett. **100**, 016401 (2008).

54 J. Pohl, and K. Albe, Phys. Rev. B **87**, 245203 (2013).

55 M. Igalson, M. Cwil, and M. Edoff, Thin Solid Films **515**, 6142 (2007).

56 T. P. Weiss, F. Ehre, V. Serrano-Escalante, T. Wang, and S. Siebentritt, Sol. RRL **5**, 2100063 (2021).

57 T. Trupke, R. A. Bardos, M. D. Abbott, and J. E. Cotter, Appl. Phys. Lett. **87**, 093503 (2005).

58 F. Babbe, L. Choubrac, and S. Siebentritt, Sol. RRL **2**, 1800248 (2018).

59 R. Scheer, and H. W. Schock, *Chalcogenide Photovoltaics: Physics*, *Technologies*, *and Thin Film Devices* (Weinheim, Wiley-VCH, 2011).

60 T. P. Weiss, O. Ramírez, S. Paetel, W.Witte, J. Nishinaga, T. Feurer, and S. Siebentritt, arXiv: 2205.00826.

61 S. De Wolf, J. Holovsky, S. J. Moon, P. Löper, B. Niesen, M. Ledinsky, F. J. Haug, J. H. Yum, and C. Ballif, J. Phys. Chem. Lett. **5**, 1035 (2014).

62 M. H. Wolter, R. Carron, E. Avancini, B. Bissig, T. P. Weiss, S. Nishiwaki, T. Feurer, S. Buecheler, P. Jackson, W. Witte, and S. Siebentritt, Prog. Photovol. **30**, 702 (2022).

63 H. Sumi, and Y. Toyozawa, J. Phys. Soc. Jpn. **31**, 342 (1971).

64 M. V. Kurik, Phys. Stat. Sol. (a) **8**, 9 (1971).

65 T. Skettrup, Phys. Rev. B **18**, 2622 (1978).

66 S. R. Johnson, and T. Tiedje, J. Appl. Phys. **78**, 5609 (1995).

67 G. D. Cody, T. Tiedje, B. Abeles, B. Brooks, and Y. Goldstein, Phys. Rev. Lett. **47**, 1480 (1981).

68 C. Ayik, I. Studenyak, M. Kranjec, and M. Kurik, Optics **4**, 76 (2014).

69 S. Siebentritt, L. Gütay, D. Regesch, Y. Aida, and V. Deprédurand, Sol. Energy Mater. Sol. Cells **119**, 18 (2013).

70 C. S. Schnohr, S. Eckner, P. Schöppe, E. Haubold, F. d'Acapito, D. Greiner, and C. A. Kaufmann, Acta Mater. **153**, 8 (2018).

71 J. K. Larsen, K. Burger, L. Gütay, and S. Siebentritt, in *Temperature dependence of potential fluctuations in chalcopyrites: Proceedings of the in 37th IEEE Photovoltaic Specialist Conference*, Seattle, 2011, pp. 396-401.

72 S. Siebentritt, Sol. Energy Mater. Sol. Cells **95**, 1471 (2011).

73 S. Siebentritt, E. Avancini, M. Bär, J. Bombsch, E. Bourgeois, S. Buecheler, R. Carron, C. Castro, S. Duguay, R. Félix, E. Handick, D. Hariskos, V. Havu, P. Jackson, H. Komsa, T. Kunze, M. Malitckaya, R. Menozzi, M. Nesladek, N. Nicoara, M. Puska, M. Raghuwanshi, P. Pareige, S. Sadewasser, G. Sozzi, A. N. Tiwari, S. Ueda, A. Vilalta-Clemente, T. P. Weiss, F. Werner, R. G. Wilks, W. Witte, and M. H. Wolter, Adv. Energy Mater. **10**, 1903752 (2020).

74 W. B. Jackson, and N. M. Amer, Phys. Rev. B **25**, 5559 (1982).

75 M. Vaněček, J. Kočka, J. Stuchlík, and A. Tříska, Solid State Commun. **39**, 1199 (1981).

76 E. Daub, and P. Würfel, Phys. Rev. Lett. **74**, 1020 (1995).

77 G. Rey, C. Spindler, F. Babbe, W. Rachad, S. Siebentritt, M. Nuys, R. Carius, S. Li, and C. Platzer-Björkman, Phys. Rev. Appl. **9**, 064008 (2018).

78 U. Rau, and J. H. Werner, Appl. Phys. Lett. **84**, 3735 (2004).

79 U. Rau, B. Blank, T. C. Müller, and T. Kirchartz, Phys. Rev. Appl. **7**, 044016 (2017).

80 G. Rey, G. Larramona, S. Bourdais, C. Choné, B. Delatouche, A. Jacob, G. Dennler, and S. Siebentritt, Sol. Energy Mater. Sol. Cells **179**, 142 (2018).

81 E. M. Spaans, J. de Wild, T. J. Savenije, and B. Vermang, J. Appl. Phys. **130**, 123103 (2021).

82 S. Siebentritt, U. Rau, S. Gharabeiki, T. P. Weiss, A. Prot, T. Wang, D. Adeleye, M. Drahem, and A. Singh, Faraday Discuss., doi: 10.1039/d2fd00057a.

83 F. Werner, M. H. Wolter, S. Siebentritt, G. Sozzi, S. Di Napoli, R. Menozzi, P. Jackson, W. Witte, R. Carron, E. Avancini, T. P. Weiss, and S. Buecheler, Prog. Photovolt.-Res. Appl. **26**, 911 (2018).

84 D. W. Niles, K. Ramanathan, J. Granata, F. Hasoon, R. Noufi, B. J. Tielsch, and J. E. Fulghum, Vacuum Sci. Tech. A **15**, 3044 (1997).

85 A. Rockett, J. S. Britt, T. Gillespie, C. Marshall, M. M. Al Jassim, F. Hasoon, R. Matson, and B. Basol, Thin Solid Films **372**, 212 (2000).

86 F. Pianezzi, P. Reinhard, A. Chirilă, B. Bissig, S. Nishiwaki, S. Buecheler, and A. N. Tiwari, Phys. Chem. Chem. Phys. **16**, 8843 (2014).

87 D. Rudmann, A. F. da Cunha, M. Kaelin, F. Kurdesau, H. Zogg, A. N. Tiwari, and G. Bilger, Appl. Phys. Lett. **84**, 1129 (2004).

88 M. Ruckh, D. Schmid, M. Kaiser, R. Schaffler, T. Walter, and H. Schock, Sol. Energy Mater. Sol. Cells **41-42**, 335 (1996).

89 L. Kronik, D. Cahen, and H. W. Schock, Adv. Mater. **10**, 31 (1998).

90 D. Abou-Ras, S. S. Schmidt, R. Caballero, T. Unold, H. W. Schock, C. T. Koch, B. Schaffer, M. Schaffer, P. P. Choi, and O. Cojocaru-Mirédin, Adv. Energy Mater. **2**, 992 (2012).

91 M. A. Contreras, B. Egaas, P. C. Dippo, J. Webb, J. Granata, K. Ramanathan, S. Asher, A. Swartzlander, and R. Noufi, in *On the role of Na and modifications to Cu(In,Ga)Se₂ absorber materials using thin-MF (M=Na, K, Cs) precursor layers: Proceedings of the Conference Record of the Twenty Sixth IEEE Photovoltaic Specialists Conference*, Anaheim, 1997, pp. 359-362.

92 Z. K. Yuan, S. Chen, Y. Xie, J. S. Park, H. Xiang, X. G. Gong, and S. H. Wei, Adv. Energy Mater. **6**, 1601191 (2016).

93 J. Hedstrom, H. Ohlsen, M. Bodegard, A. Kylner, L. Stolt, D. Hariskos, M. Ruckh, and H.-W. Schock, in *ZnO/CdS/Cu(In,Ga)Se₂ thin film solar cells with improved performance: Proceedings of the in Conference Record of the Twenty Third IEEE Photovoltaic Specialists Conference*, Louisville, 1993.

94 D. Colombara, F. Werner, T. Schwarz, I. Cañero Infante, Y. Fleming, N. Valle, C. Spindler, E. Vacchieri, G. Rey, M. Guennou, M. Bouttemy, A. G. Manjón, I. Peral Alonso, M. Melchiorre, B. El Adib, B. Gault, D. Raabe, P. J. Dale, and S. Siebentritt, Nat. Commun. **9**, 826 (2018).

95 D. Rudmann, D. Brémaud, A. F. da Cunha, G. Bilger, A. Strohm, M. Kaelin, H. Zogg, and A. N. Tiwari, Thin Solid Films **480-481**, 55 (2005).

96 S. Zahedi-Azad, M. Maiberg, and R. Scheer, Prog. Photovolt.-Res. Appl. **28**, 1146 (2020).

97 A. Chirilă, P. Reinhard, F. Pianezzi, P. Bloesch, A. R. Uhl, C. Fella, L. Kranz, D. Keller, C. Gretener, H. Hagendorfer, D. Jaeger, R. Erni, S. Nishiwaki, S. Buecheler, and A. N. Tiwari, Nat. Mater. **12**, 1107 (2013).

98 P. Reinhard, F. Pianezzi, B. Bissig, A. Chirila, P. Blosch, S. Nishiwaki, S. Buecheler, and A. N. Tiwari, IEEE J. Photovol. **5**, 656 (2015).

99 P. Pistor, D. Greiner, C. A. Kaufmann, S. Brunken, M. Gorgoi, A. Steigert, W. Calvet, I. Lauermann, R. Klenk, T. Unold, and M. C. Lux-Steiner, Appl. Phys. Lett. **105**, 063901 (2014).

100 T. Kato, A. Handa, T. Yagioka, T. Matsuura, K. Yamamoto, S. Higashi, J. L. Wu, K. F. Tai, H. Hiroi, T. Yoshiyama, T. Sakai, and H.

Sugimoto, IEEE J. Photovol. **7**, 1773 (2017).

101 E. Handick, P. Reinhard, R. G. Wilks, F. Pianezzi, T. Kunze, D. Kreikemeyer-Lorenzo, L. Weinhardt, M. Blum, W. Yang, M. Gorgoi, E. Ikenaga, D. Gerlach, S. Ueda, Y. Yamashita, T. Chikyow, C. Heske, S. Buecheler, A. N. Tiwari, and M. Bär, ACS Appl. Mater. Interfaces **9**, 3581 (2017).

102 T. Lepetit, S. Harel, L. Arzel, G. Ouvrard, and N. Barreau, IEEE J. Photovol. **6**, 1316 (2016).

103 P. Reinhard, B. Bissig, F. Pianezzi, H. Hagendorfer, G. Sozzi, R. Menozzi, C. Gretener, S. Nishiwaki, S. Buecheler, and A. N. Tiwari, Nano Lett. **15**, 3334 (2015).

104 T. Lepetit, *Influence of KF Post Deposition Treatment on the Poly-crystalline Cu(In,Ga)Se$_2$/CdS Heterojunction Formation For Photovoltaic Application*, Dissertation for the Doctoral Degree (University of Nantes, Nantes, 2015).

105 E. Avancini, R. Carron, T. P. Weiss, C. Andres, M. Bürki, C. Schreiner, R. Figi, Y. E. Romanyuk, S. Buecheler, and A. N. Tiwari, Chem. Mater. **29**, 9695 (2017).

106 N. Taguchi, S. Tanaka, and S. Ishizuka, Appl. Phys. Lett. **113**, 113903 (2018).

107 T. Kodalle, T. Bertram, R. Schlatmann, and C. A. Kaufmann, IEEE J. Photovol. **9**, 1839 (2019).

108 T. Kodalle, M. D. Heinemann, D. Greiner, H. A. Yetkin, M. Klupsch, C. Li, P. A. van Aken, I. Lauermann, R. Schlatmann, and C. A. Kaufmann, Sol. RRL **2**, 1800156 (2018).

109 T. P. Weiss, S. Nishiwaki, B. Bissig, R. Carron, E. Avancini, J. Löckinger, S. Buecheler, and A. N. Tiwari, Adv. Mater. Interfaces **5**, 1701007 (2018).

110 M. Malitckaya, H. P. Komsa, V. Havu, and M. J. Puska, J. Phys. Chem. C **121**, 15516 (2017).

111 E. Handick, P. Reinhard, J. H. Alsmeier, L. Köhler, F. Pianezzi, S. Krause, M. Gorgoi, E. Ikenaga, N. Koch, R. G. Wilks, S. Buecheler, A. N. Tiwari, and M. Bär, ACS Appl. Mater. Interfaces **7**, 27414 (2015).

112 M. Morkel, L. Weinhardt, B. Lohmüller, C. Heske, E. Umbach, W. Riedl, S. Zweigart, and F. Karg, Appl. Phys. Lett. **79**, 4482 (2001).

113 M. Bär, S. Nishiwaki, L. Weinhardt, S. Pookpanratana, O. Fuchs, M. Blum, W. Yang, J. D. Denlinger, W. N. Shafarman, and C. Heske, Appl. Phys. Lett. **93**, 244103 (2008).

114 S. Ishizuka, H. Shibata, J. Nishinaga, Y. Kamikawa, and P. J. Fons, Appl. Phys. Lett. **113**, 063901 (2018).

115 J. V. Li, S. Grover, M. A. Contreras, K. Ramanathan, D. Kuciauskas, and R. Noufi, Sol. Energy Mater. Sol. Cells **124**, 143 (2014).

116 R. Scheer, J. Appl. Phys. **105**, 104505 (2009).

117 M. Sood, A. Urbaniak, C. Kameni Boumenou, T. P. Weiss, H. Elanzeery, F. Babbe, F. Werner, M. Melchiorre, and S. Siebentritt, Prog. Photovol. **30**, 263 (2022).

118 N. Nicoara, R. Manaligod, P. Jackson, D. Hariskos, W. Witte, G. Sozzi, R. Menozzi, and S. Sadewasser, Nat. Commun. **10**, 3980 (2019).

119 M. Krause, A. Nikolaeva, M. Maiberg, P. Jackson, D. Hariskos, W. Witte, J. A. Márquez, S. Levcenko, T. Unold, R. Scheer, and D. Abou-Ras, Nat. Commun. **11**, 4189 (2020).

120 A. Vilalta-Clemente, M. Raghuwanshi, S. Duguay, C. Castro, E. Cadel, P. Pareige, P. Jackson, R. Wuerz, D. Hariskos, and W. Witte, Appl. Phys. Lett. **112**, 103105 (2018).

121 D. Abou-Ras, A. Nikolaeva, S. Caicedo Dávila, M. Krause, H. Guthrey, M. Al-Jassim, M. Morawski, and R. Scheer, Sol. RRL **3**, 1900095 (2019).

122 O. Ramírez, M. Bertrand, A. Debot, D. Siopa, N. Valle, J. Schmauch, M. Melchiorre, and S. Siebentritt, Sol. RRL **5**, 2000727 (2021).

123 O. Ramírez, J. Nishinaga, F. Dingwell, T. Wang, A. Prot, M. H. Wolter, V. Ranjan, and S. Siebentritt, arXiv: 2212.01603.

124 J. E. Avon, K. Yoodee, and J. C. Woolley, J. Appl. Phys. **55**, 524 (1984).

125 G. M. Hanket, J. H. Boyle, and W. N. Shafarman, in *Characterization and device performance of (AgCu)(InGa)Se$_2$ absorber layers:*

Proceedings of the in 2009 34th IEEE Photovoltaic Specialists Conference (PVSC), Philadelphia, 2009.

126 G. M. Hanket, J. H. Boyle, W. N. Shafarman, and G. Teeter, in *Wide-bandgap (AgCu)(InGa)Se$_2$ absorber layers deposited by three-stage co-evaporation: Proceedings of the in 2010 35th IEEE Photovoltaic Specialists Conference*, Honolulu, 2010.

127 J. H. Boyle, B. E. McCandless, W. N. Shafarman, and R. W. Birkmire, J. Appl. Phys. **115**, 223504 (2014).

128 W. Shafarman, C. Thompson, J. Boyle, G. Hanket, P. Erslev, and J. D. Cohen, in *Device characterization of (AgCu)(InGa)Se$_2$ solar cells: Proceedings of the in 2010 35th IEEE Photovoltaic Specialists Conference*, Honolulu, 2010.

129 K. V. Sopiha, J. K. Larsen, O. Donzel-Gargand, F. Khavari, J. Keller, M. Edoff, C. Platzer-Björkman, C. Persson, and J. J. S. Scragg, J. Mater. Chem. A **8**, 8740 (2020).

130 J. Keller, L. Stolt, K. V. Sopiha, J. K. Larsen, L. Riekehr, and M. Edoff, Sol. RRL **4**, 2000508 (2020).

131 J. Keller, K. V. Sopiha, O. Stolt, L. Stolt, C. Persson, J. J. S. Scragg, T. Törndahl, and M. Edoff, Prog. Photovolt. Res. Appl. **28**, 237 (2020).

132 L. Chen, J. W. Lee, and W. N. Shafarman, IEEE J. Photovol. **4**, 447 (2014).

133 S. Essig, S. Paetel, T. M. Friedlmeier, and M. Powalla, J. Phys. Mater. **4**, 024003 (2021).

134 L. Chen, S. Soltanmohammad, J. W. Lee, B. E. McCandless, and W. N. Shafarman, Sol. Energy Mater. Sol. Cells **166**, 18 (2017).

135 N. Valdes, J. W. Lee, and W. Shafarman, Sol. Energy Mater. Sol. Cells **195**, 155 (2019).

136 M. Edoff, T. Jarmar, N. S. Nilsson, E. Wallin, D. Hogstrom, O. Stolt, O. Lundberg, W. Shafarman, and L. Stolt, IEEE J. Photovol. **7**, 1789 (2017).

137 S. C. Yang, J. Sastre, M. Krause, X. Sun, R. Hertwig, M. Ochoa, A. N. Tiwari, and R. Carron, Sol. RRL **5**, 2100108 (2021).

138 J. Boyle, G. Hanket, and W. Shafarman, in *Optical and quantum efficiency analysis of (Ag,Cu)(In,Ga)Se$_2$ absorber layers: Proceedings of the in 2009 34th IEEE Photovoltaic Specialists Conference (PVSC)*, Philadelphia, 2009.

139 A. Klein, J. Phys.-Condens. Matter **27**, 134201 (2015).

140 T. Nakada, K. Yamada, R. Arai, H. Ishizaki, and N. Yamada, MRS Proc. **865**, F11.1 (2005).

141 M. A. Contreras, L. M. Mansfield, B. Egaas, J. Li, M. Romero, R. Noufi, E. Rudiger-Voigt, and W. Mannstadt, Prog. Photovolt.-Res. Appl. **20**, 843 (2012).

142 P. Erslev, G. M. Hanket, W. N. Shafarman, and D. J. Cohen, MRS Proc. **1165**, 1165 (2009).

143 J. T. Heath, J. D. Cohen, W. N. Shafarman, D. X. Liao, and A. A. Rockett, Appl. Phys. Lett. **80**, 4540 (2002).

144 J. Keller, P. Pearson, N. Shariati Nilsson, O. Stolt, L. Stolt, and M. Edoff, Sol. RRL **5**, 2100403 (2021).

145 C. P. Thompson, L. Chen, W. N. Shafarman, J. Lee, S. Fields, and R. W. Birkmire, in *Bandgap gradients in (Ag,Cu)(In,Ga)Se$_2$ thin film solar cells deposited by three-stage co-evaporation: Proceedings of the in 2015 IEEE 42nd Photovoltaic Specialist Conference (PVSC)*, New Orleans, 2015.

146 N. H. Valdes, J. W. Lee, and W. N. Shafarman, IEEE J. Photovol. **9**, 906 (2019).

147 G. Kim, W. M. Kim, J. K. Park, D. Kim, H. Yu, and J. H. Jeong, ACS Appl. Mater. Interfaces **11**, 31923 (2019).

148 P. Caprioglio, C. M. Wolff, O. J. Sandberg, A. Armin, B. Rech, S. Albrecht, D. Neher, and M. Stolterfoht, Adv. Energy Mater. **10**, 2000502 (2020).

149 M. Hermle, F. Feldmann, M. Bivour, J. C. Goldschmidt, and S. W. Glunz, Appl. Phys. Rev. **7**, 021305 (2020).

150 T. Wang, F. Ehre, T. P. Weiss, B. Veith-Wolf, V. Titova, N. Valle, M. Melchiorre, O. Ramirez, J. Schmidt, and S. Siebentritt, Adv. Energy Mat. **2022**, 2202076 (2022).

151 T. P. Weiss, R. Carron, M. H. Wolter, J. Löckinger, E. Avancini, S.

Siebentritt, S. Buecheler, and A. N. Tiwari, Sci. Tech. Adv. Mater. **20**, 313 (2019).

152 T. T. Werner, G. M. Mudd, and S. M. Jowitt, Ore Geol. Rev. **86**, 939 (2017).

153 O. Lundberg, M. Bodegård, J. Malmström, and L. Stolt, Prog. Photovolt.-Res. Appl. **11**, 77 (2003).

154 G. Baraldi, R. Caballero, C. A. Kaufmann, and J. Gonzalo, Energy Procedia **10**, 38 (2011).

155 N. Dahan, Z. Jehl, T. Hildebrandt, J. J. Greffet, J. F. Guillemoles, D. Lincot, and N. Naghavi, J. Appl. Phys. **112**, 094902 (2012).

156 J. G. Mutitu, U. Obahiagbon, S. Shi, W. Shafarman, and D. W. Prather, IEEE J. Photovol. **4**, 948 (2014).

157 C. van Lare, G. Yin, A. Polman, and M. Schmid, ACS Nano **9**, 9603 (2015).

158 F. Mollica, M. Jubault, F. Donsanti, A. Loubat, M. Bouttemy, A. Etcheberry, and N. Naghavi, Thin Solid Films **633**, 202 (2017).

159 B. Bissig, R. Carron, L. Greuter, S. Nishiwaki, E. Avancini, C. Andres, T. Feurer, S. Buecheler, and A. N. Tiwari, Prog. Photovolt.-Res. Appl. **26**, 894 (2018).

160 B. Vermang, V. Fjällström, J. Pettersson, P. Salomé, and M. Edoff, Sol. Energy Mater. Sol. Cells **117**, 505 (2013).

161 E. Jarzembowski, B. Fuhrmann, H. Leipner, W. Fränzel, and R. Scheer, Thin Solid Films **633**, 61 (2017).

162 F. Mollica, J. Goffard, M. Jubault, F. Donsanti, S. Collin, A. Cattoni, L. Lombez, and N. Naghavi, in *Comparative study of patterned TiO₂ and Al₂O₃ layers as passivated back-contact for ultra-thin Cu(In, Ga)Se₂ solar cells: Proceedings of the in 2016 IEEE 43rd Photovoltaic Specialists Conference (PVSC)*, Portland, 2016.

163 B. Vermang, J. T. Watjen, C. Frisk, V. Fjallstrom, F. Rostvall, M. Edoff, P. Salome, J. Borme, N. Nicoara, and S. Sadewasser, IEEE J. Photovol. **4**, 1644 (2014).

164 G. Birant, J. de Wild, M. Meuris, J. Poortmans, and B. Vermang, Appl. Sci. **9**, 677 (2019).

165 F. Werner, B. Veith-Wolf, C. Spindler, M. R. Barget, F. Babbe, J. Guillot, J. Schmidt, and S. Siebentritt, Phys. Rev. Appl. **13**, 054004 (2020).

166 S. Albrecht, and B. Rech, Nat. Energy **2**, 16196 (2017).

167 G. E. Eperon, M. T. Hörantner, and H. J. Snaith, Nat. Rev. Chem. **1**, 0095 (2017).

168 F. Lang, M. Jošt, K. Frohna, E. Köhnen, A. Al-Ashouri, A. R. Bowman, T. Bertram, A. B. Morales-Vilches, D. Koushik, E. M. Tennyson, K. Galkowski, G. Landi, M. Creatore, B. Stannowski, C. A. Kaufmann, J. Bundesmann, J. Rappich, B. Rech, A. Denker, S. Albrecht, H. C. Neitzert, N. H. Nickel, and S. D. Stranks, Joule **4**, 1054 (2020).

169 M. Jošt, E. Köhnen, A. Al-Ashouri, T. Bertram, Š. Tomšič, A. Magomedov, E. Kasparavicius, T. Kodalle, B. Lipovšek, V. Getautis, R. Schlatmann, C. A. Kaufmann, S. Albrecht, and M. Topič, ACS Energy Lett. **7**, 1298 (2022).

170 S. Gharibzadeh, I. M. Hossain, P. Fassl, B. A. Nejand, T. Abzieher, M. Schultes, E. Ahlswede, P. Jackson, M. Powalla, S. Schäfer, M. Rienäcker, T. Wietler, R. Peibst, U. Lemmer, B. S. Richards, and U. W. Paetzold, Adv. Funct. Mater. **30**, 1909919 (2020).

171 M. Nakamura, C. C. Lin, C. Nishiyama, K. Tada, T. Bessho, and H. Segawa, ACS Appl. Energy Mater. **5**, 8103 (2022).

172 K. Makita, Y. Kamikawa, H. Mizuno, R. Oshima, Y. Shoji, S. Ishi-zuka, R. Muller, D. Lackner, F. Dimroth, and T. Sugaya, IEEE J. Photovol. **12**, 639 (2022).

173 T. Feurer, R. Carron, G. Torres Sevilla, F. Fu, S. Pisoni, Y. E. Romanyuk, S. Buecheler, and A. N. Tiwari, Adv. Energy Mater. **9**, 1901428 (2019).

174 S. Nishiwaki, S. Siebentritt, P. Walk, and M. C. Lux-Steiner, Prog. Photovolt-Res. Appl. **11**, 243 (2003).

175 A. Onno, N. Rodkey, A. Asgharzadeh, S. Manzoor, Z. J. Yu, F. Toor, and Z. C. Holman, Joule **4**, 580 (2020).

176 W. Witte, D. Hariskos, S. Paetel, M. Maiberg, S. Zahedi-Azad, P. Pistor, H. Kempa, R. Scheer, D. Hauschild, V. van Maris, M. Blankenship, L. Weinhardt, C. Heske, J. Keutgen, O. Cojocaru-Mirédin, E. Ghorbani, K. Albe, X. Jin, R. Schneider, D. Gerthsen, A. Nikolaeva, J. A. Marquez-Prieto, M. Krause, S. Schäfer, D. Abou-Ras, T. Unold, R. Mainz, J. Seeger, F. Wilhelmi, M. Hetterich, M. Schweiger, B. Dimmler, and M. Powalla, CIGS Devices with Increased Bandgap Energy: Results of the EFFCIS Project, EU PVSEC Programme Online, 2021, https://www.photovoltaic-conference.com/programme/conference.html.

177 H. Hiroi, Y. Iwata, S. Adachi, H. Sugimoto, and A. Yamada, IEEE J. Photovol. **6**, 760 (2016).

178 S. Shukla, M. Sood, D. Adeleye, S. Peedle, G. Kusch, D. Dahliah, M. Melchiorre, G. M. Rignanese, G. Hautier, R. Oliver, and S. Siebentritt, Joule **5**, 1816 (2021).

179 F. Larsson, N. S. Nilsson, J. Keller, C. Frisk, V. Kosyak, M. Edoff, and T. Törndahl, Prog. Photovolt.-Res. Appl. **25**, 755 (2017).

180 N. Barreau, A. Thomere, D. Cammilleri, A. Crossay, C. Guillot-Deudon, A. Lafond, N. Stéphant; D. Lincot, M. T. Caldes, R. Bodeuxn, and B. Bérenguier, in *High efficiency solar cell based on Cu(In,Ga)S₂ thin film grown by 3-stage process: Proceedings of the in 2020 47th IEEE Photovoltaic Specialists Conference (PVSC)*, Calgary, 2020.

181 T. J. Coutts, J. S. Ward, D. L. Young, K. A. Emery, T. A. Gessert, and R. Noufi, Prog. Photovolt.-Res. Appl. **11**, 359 (2003).

182 T. P. White, N. N. Lal, and K. R. Catchpole, IEEE J. Photovol. **4**, 208 (2014).

183 M. Sood, P. Gnanasambandan, D. Adeleye, S. Shukla, N. Adjeroud, R. Leturcq, and S. Siebentritt, J. Phys. Energy **4**, 045005 (2022).

184 M. Sood, D. Adeleye, S. Shukla, T. Törndahl, A. Hultqvist, and S. Siebentritt, Faraday Discuss. **239**, 328 (2022).

185 P. O. Grabitz, U. Rau, and J. H. Werner, Thin Solid Films **487**, 14 (2005).

186 T. P. Weiss, B. Bissig, T. Feurer, R. Carron, S. Buecheler, and A. N. Tiwari, Sci. Rep. **9**, 5385 (2019).

187 D. Colombara, H. Elanzeery, N. Nicoara, D. Sharma, M. Claro, T. Schwarz, A. Koprek, M. H. Wolter, M. Melchiorre, M. Sood, N. Valle, O. Bondarchuk, F. Babbe, C. Spindler, O. Cojocaru-Miredin, D. Raabe, P. J. Dale, S. Sadewasser, and S. Siebentritt, Nat. Commun. **11**, 3634 (2020).

188 H. Elanzeery, M. Melchiorre, M. Sood, F. Babbe, F. Werner, G. Brammertz, and S. Siebentritt, Phys. Rev. Mater. **3**, 055403 (2019).

189 I. M. Peters, C. D. Rodriguez Gallegos, S. E. Sofia, and T. Buonassisi, Joule **3**, 2732 (2019).

190 S. E. Sofia, J. P. Mailoa, D. N. Weiss, B. J. Stanbery, T. Buonassisi, and I. M. Peters, Nat. Energy **3**, 387 (2018).